RSC Advances

ROYAL SOCIETY OF CHEMISTRY

PAPER

View Article Online
View Journal | View Issue

Cite this: *RSC Adv.*, 2025, **15**, 26787

Visible-light-driven Z-scheme tungsten oxide/ silver phosphate/ coffee bean biochar photocatalyst for simultaneous degradation of ciprofloxacin and chlorpyrifos†

Debasis Nanda,[a] Chirasmayee Mohanty,[a] Amrita Priyadarsini,[b] Nigamananda Das,[a] Manjusri Misra,[c] Amar K. Mohanty[c] and Ajaya K. Behera*[ad]

Received 25th June 2025
Accepted 22nd July 2025

DOI: 10.1039/d5ra04526f

rsc.li/rsc-advances

The integration of biochar as a solid-state electron mediator in Z-scheme photocatalytic systems represents a promising approach for the efficient degradation of organic contaminants. In this study, a novel magnetic Z-scheme photocatalyst, silver phosphate–tungsten oxide (Ag_3PO_4–WO_3)/coffee bean biochar composite (ABW-10), was synthesized *via* a hydrothermal method. Ag_3PO_4 and WO_3 were immobilized onto biochar layers to facilitate charge separation and enhance electron transfer under visible light irradiation. Morphological analysis confirmed a uniformly decorated biochar surface with well-dispersed nanoparticles, supporting efficient photocatalytic performance. Mott–Schottky plots revealed improved charge carrier dynamics and conductivity. Radical scavenging experiments validated the Z-scheme charge transfer mechanism, confirming the generation of reactive oxygen species. ABW-10 exhibited exceptional photocatalytic activity, achieving nearly 100% mineralization of ciprofloxacin (50 ppm) and chlorpyrifos (20 ppm) within 60 minutes under ambient conditions at a catalyst dosage of 0.1 g. LC-MS analysis elucidated the degradation pathways of both pollutants. Additionally, the composite demonstrated excellent reusability and a fivefold increase in antimicrobial activity against both *Staphylococcus aureus* and *Escherichia coli* compared to the individual components.

1. Introduction

The exponential growth in the global population, rapid urbanization, and accelerated industrialization have exerted unprecedented pressure on water resources. Human activities, including the discharge of industrial effluents, agricultural runoff, and untreated municipal waste, have turned vital water bodies into reservoirs of hazardous contaminants, severely compromising water quality and limiting access to clean and safe water.[1] As the demand for potable water continues to rise, innovative and sustainable strategies to restore and protect aquatic ecosystems are urgently required.[2,3] Among the diverse pollutants, antibiotics, pesticides, and pathogenic microorganisms pose significant environmental and health challenges. The widespread and indiscriminate use of antibiotics, such as ciprofloxacin, in human and veterinary medicine has led to their accumulation in aquatic environments due to poor metabolization rates. These compounds persist in wastewater and surface waters at concentrations ranging from ng L^{-1} to μg L^{-1}, exhibiting toxic, mutagenic, and carcinogenic properties that conventional sewage treatment plants struggle to remove.[4–6] Photocatalytic degradation has emerged as a promising strategy for breaking down such persistent pharmaceutical pollutants.[7,8]

Pesticide contamination, particularly from organophosphates like chlorpyrifos (CPF), further exacerbates environmental degradation. Despite its widespread agricultural use, only a small fraction (0.1%) of applied chlorpyrifos reaches target pests, with the remainder dispersing into the environment, leading to groundwater contamination and ecological disruption.[9,10] CPF's long environmental half-life (60–120 days) and neurotoxic effects, particularly on children and fetuses, necessitate effective remediation strategies.[11,12] Bioremediation using native and resistant microbial communities offers an eco-friendly and efficient solution for the restoration of pesticide-

---

[a] *Department of Chemistry, Utkal University, Bhubaneswar, Odisha, 751004, India. E-mail: ajayabehera@utkaluniversity.ac.in; Fax: +91 0674 2581850; Tel: +91-8280098214*

[b] *Department of Chemistry, College of Basic Science and Humanities, Odisha University of Agriculture and Technology, Odisha, India*

[c] *Bioproducts Discovery and Development Centre, Department of Plant Agriculture, Crop Science Building, University of Guelph, Guelph, Ontario, Canada*

[d] *Centre of Excellence in Advanced Materials and Applications, Utkal University, Bhubaneswar, 751 004, India*

† Electronic supplementary information (ESI) available. See DOI: **https://doi.org/10.1039/d5ra04526f**

contaminated soils.[13,14] In parallel, pathogenic contamination by bacteria such as *Escherichia coli* and *Staphylococcus aureus* poses a serious public health risk, particularly in low-income countries, where it contributes to waterborne diseases and severe health complications.[15,16] The urgent need for economical and eco-friendly solutions to combat pathogenic contamination has gained renewed attention, especially in the wake of the global pandemic.

Advanced nanocomposite materials have emerged as transformative solutions for addressing these environmental challenges. Silver phosphate (Ag_3PO_4) is known for its high photocatalytic efficiency under visible light irradiation.[17] However, its practical application is hindered by photodegradation, where photo-generated electrons reduce silver ions to metallic silver, leading to the deterioration of photocatalytic activity.[18] Recent studies have demonstrated that coupling Ag_3PO_4 with other semiconductors can improve charge separation and stability.[19] Among these, tungstate oxide (WO_3) stands out for its remarkable photocatalytic properties, exceptional stability, and light absorption capabilities in the visible and ultraviolet spectrum.[20]

Incorporating biochar as a ESI† for Ag_3PO_4 and WO_3 offers a novel approach to enhancing photocatalytic performance, as supported by different studies demonstrating the effective coupling of photocatalysts with carbonaceous materials to improve charge separation and stability.[21,22] Biochar, derived from biomass pyrolysis, provides high surface area, porosity, and excellent adsorption capacity, facilitating the immobilization of nanoparticles and improving photocatalytic stability.[23] This synergistic system of Ag_3PO_4/WO_3/biochar nanocomposite demonstrates enhanced photocatalytic activity, efficient pollutant degradation, and easy recovery of the photocatalyst. Biochar's stable chemical properties and π-conjugated structure enable dynamic electron transfer, further enhancing the photocatalytic process.

This study explores the potential of the Ag_3PO_4/WO_3/biochar nanocomposite for visible light-driven degradation of aquatic pollutants, addressing critical environmental challenges and contributing to sustainable water treatment solutions.

2. Experimental section

2.1 Reagents

The primary raw material used in this research was waste coffee beans collected from the foothills of the Deomali range in the Koraput region of Odisha. Various high-purity chemicals were employed throughout the study to ensure precise synthesis and characterization processes. These included silver nitrate ($AgNO_3$), ciprofloxacin (CPX), sodium tungstate dihydrate ($Na_2WO_4 \cdot 2H_2O$), sodium sulfate (Na_2SO_4), chlorpyrifos (CPF), benzoquinone (BQ), isopropanol (IPA), potassium dichromate ($K_2Cr_2O_7$), and disodium ethylenediaminetetraacetate (Na_2EDTA), all sourced from Sigma Aldrich with an assay purity of 99.0%. Additionally, ethanol and concentrated hydrochloric acid (HCl), also with 99.0% assay purity, were procured from Himedia. Double-distilled water was meticulously used to prepare all aqueous solutions for the synthesis process, ensuring high-quality results in the development of hybrid nanocomposites.

2.2. Synthesis of biochar

Meticulous procedures were followed to prepare the coffee bean biomass for subsequent examination and applications. To ensure the integrity of the biomass, it was initially washed with tap water and then thoroughly rinsed with distilled water to remove surface impurities. The cleaned biomass was carefully sectioned into smaller pieces to maximize surface area for further treatments. Moisture content was effectively eliminated by drying the material in an oven at 100 °C until a constant weight was achieved, a critical step for subsequent processing. The dried biomass was finely ground using a pulveriser fitted with a 250 mm mesh, ensuring uniformity and enhanced reactivity. The key synthesis step, pyrolysis, was conducted in a muffle furnace at 500 °C for one hour under a continuous nitrogen gas flow, with a controlled heating rate of 10 °C min^{-1}. This controlled thermal decomposition process was essential in transforming the biomass into a functional material, establishing a foundation for its potential applications in diverse environmental and industrial fields.

2.3. Synthesis of silver phosphate (Ag_3PO_4)

For the synthesis of silver phosphate, solutions of $AgNO_3$ (0.3 M, 1.27 g) and $(NH_4)_2H_2PO_4$ (0.45 M, 1.29 g) were prepared separately in beakers. The $(NH_4)_2H_2PO_4$ solution was carefully added to the $AgNO_3$ solution over four hours at 50 °C with continuous stirring, resulting in the formation of a distinct yellow precipitate. The silver phosphate obtained was thoroughly washed with a 75/25 (v/v%) ethanol–water solution to remove any residual impurities. This vigorous cleaning process ensured the purity of the synthesized product. The washed material was then dried at 70 °C overnight, yielding clean and stable silver phosphate for further characterization and applications.

2.4. Synthesis of tungstate oxide (WO_3)

The synthesis of tungstate oxide (WO_3) was accomplished through a multistep process. Initially, 2.5 grams of sodium tungstate dihydrate was dissolved in 40 mL of deionized water under mild stirring to form a homogeneous solution. To this solution, 4 grams of sodium sulfate (Na_2SO_4) were added, ensuring uniform mixing. The pH of the suspension was meticulously adjusted to 1.5 by the gradual addition of concentrated hydrochloric acid (HCl). Following pH regulation, the solution was transferred to a 50 mL Teflon-lined stainless-steel autoclave, which was sealed and subjected to hydrothermal treatment at 180 °C for 5 hours. After cooling to room temperature, the sample was carefully extracted and thoroughly washed with ethanol and deionized water to eliminate any residual impurities. The purified product was then dried overnight at 80 °C, yielding high-purity tungstate oxide (WO_3) for further applications.

2.5. Synthesis of Z-scheme nanocomposite (Ag_3PO_4/WO_3/biochar) ABW-10

A two-step synthesis method was employed to prepare tungsten oxide (WO_3)/silver phosphate (Ag_3PO_4)/biochar hybrid composites with a stoichiometric biochar/Ag_3PO_4 content of 10 wt%. In the initial step, WO_3 (80 wt%) and biochar (10 wt%) were dispersed in 20 mL of distilled water and homogenized using ultrasonic vibration for 30 minutes. Concurrently, a solution containing silver nitrate (0.3 M) and $(NH_4)_2H_2PO_4$ (0.45 M) was prepared in a three-necked round-bottom flask. The ultrasonicated WO_3/biochar dispersion was gradually added to the silver phosphate solution under continuous stirring for one hour. The mixture was then heated at 50 °C with constant stirring for 3 hours, resulting in the formation of a black solid comprising Ag_3PO_4/WO_3/biochar, maintaining a 10 wt% biochar/Ag_3PO_4 ratio. The solid product was recovered by vacuum filtration, washed thoroughly with a 70/30% (v/v) ethanol–water solution, and dried at 80 °C overnight. The resulting composite, designated as ABW-10, was subsequently evaluated for its organic pollutant mineralization efficiency. The schematic representation of the synthesis process is illustrated in Fig. 1.

2.6. Characterisation

X-ray diffraction (XRD) was used to examine the crystallinity and multiphase composition of all produced samples (PANalytical X'Pert powder diffractometer). The measurements were carried out using Cu Kα radiation with a wavelength of 1.5406 Å. The important bonds in the samples were identified using an FTIR spectrophotometer (IRAffinity-1S, Shimadzu). The optical absorption properties of the synthesized samples were investigated using UV–vis diffuse reflectance spectroscopy (Shimadzu UV-2400) equipped with an integrating sphere attachment. The measurements were carried out in the wavelength range of 200–800 nm using $BaSO_4$ as the reflectance standard. These absorbance values, plotted against wavelength, were then used to estimate the band gap energies using Tauc's plots derived from the Kubelka–Munk function, which is the standard method for band gap estimation from UV-Visible diffuse reflectance spectra (DRS). The photoluminescence (PL) spectra were scanned on an RF-6000 spectrofluorometer to investigate the photogenerated charge carrier recombination rate. A scanning electron microscope (SEM, Zeiss EVO) and a high-resolution transmission electron microscope (HRTEM, Jeol Jem F200) with a selected area electron diffraction pattern (SAED) were used for the morphological investigations. Energy dispersive X-ray spectroscopy (EDX) and elemental mapping revealed the presence of elements (Ag, W, O, C, N, and P) and their proportions. Lastly, liquid chromatography-mass spectrometry (LC-MS) measurements on a Shimadzu LC-MS/MS 8045 device with electrospray ionization mass spectrometry were used to examine the photocatalytic degradation products. This analysis revealed information about the composition and transformation of the degradation products.

3. Result and discussion

3.1. Morphological analysis

The morphology and interfacial characteristics of as-prepared photocatalyst materials, including Ag_3PO_4, WO_3, biochar, and ABW-10, were investigated using scanning electron microscopy (SEM) as shown in Fig. 2a–e. The SEM image of pure Ag_3PO_4 (Fig. 2b) reveals the presence of agglomerated quasi-spherical nanoparticles with sizes generally below 100 nm. WO_3 (Fig. 2c) exhibits rod-like and spherical morphologies ranging from ∼50–100 nm. The composite ABW-10 (Fig. 2d) shows a uniformly distributed heterostructure, indicating successful integration of all components at the nanoscale.

This integration indicated successful synthesis of the Z-scheme ABW-10 system *via* a facile hydrothermal process, with structures grown on continuous layers of biochar. However, intergranular nanoparticle aggregation was observed in the ABW-10 nanocomposite, potentially due to interfacial grain reactivity influenced by exchanging dipole moments of particles with wide surface-active sites in the system.

Transmission electron microscopy (TEM) analysis was employed to gain deeper insights into the interfacial connection between WO_3 and Ag_3PO_4 particles on the biochar layers within the ABW-10 photocatalytic system. Fig. 3a illustrates the close integration of WO_3 and Ag_3PO_4 particles with the biochar sheet. The acquired TEM images reveal the multi-layered structure of biochar, exposing numerous edges conducive to catalytic reactions. Additionally, the images demonstrate the well-ornamented biochar layers, with large WO_3 particles and tiny Ag_3PO_4 particles uniformly distributed across the surface (Fig. 3b). Unlike scanning electron microscopy (SEM), TEM analysis allows for the clear visualization of individual semiconductor catalysts, eliminating the issue of particle aggregation observed in SEM data. The precise particle sizes of individual catalysts were thus computable. Specifically, TEM analysis revealed that WO_3 particles are in direct contact with biochar layers, with sizes ranging from 100 to 300 nm. In contrast, Ag_3PO_4 nanoparticles were observed to be smaller, ranging from 10 to 30 nm, and evenly dispersed over the biochar layers.

3.2. Structural analysis

The data revealed from the HRTEM survey was found to be more compatible with the XRD data analysis, as could be found in Fig. 4. It was found that the XRD pattern of WO_3 nanoparticles depicts different peaks at $2\theta = 14.0°$, 22.78°, 28.21°, 37.62°, 49.94°, 55° of the hexagonal structure that are well matched to the (100), (001), (200), (210), (220) and (202)planes, respectively (JCPDS standard data, card no. 01-075-2187).[24] Regarding biochar, the XRD pattern displays a distinct peak at $2\theta = 30°$ because of the plane of (002). Due to the small amount of biochar present in the ABW-10 composite in the XRD examination, this peak was not apparent and was discovered in the ABW-10. Ag_3PO_4's powder diffraction pattern (JCPDS code number 06-0505) indicates that the crystal shape is cubic. Similar peak patterns can be seen in the diffraction patterns of the ABW-10 composites, including those of the Ag_3PO_4 and WO_3 peaks, Ca. (210), (220), (200), and (320), among others. This demonstrates that the ABW-10 composite was successfully formed *via* the hydrothermal technique. Fig. 4c and d shows the results of an additional inspection of the WO_3 and Ag_3PO_4 microscopic

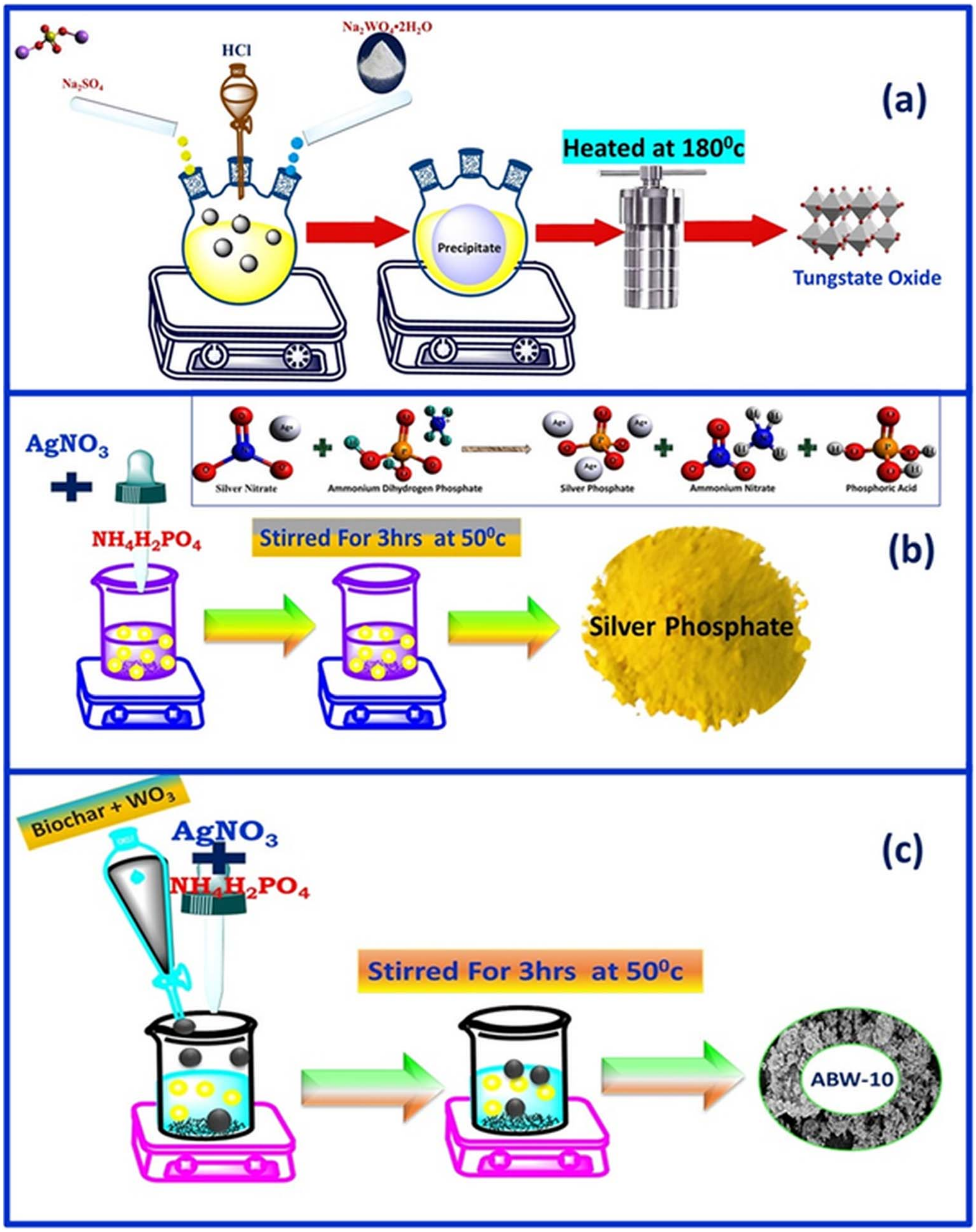

Fig. 1 Schematic presentation of the synthesis process of (a) tungstate oxide, (b) silver phosphate, and (c) ABW-10 composite.

structures using high-resolution TEM (HRTEM) images obtained from SAED. As seen in the figure, the diffraction ring pattern consists of a bright and dark pattern grouped in a ring-like configuration. The discontinuous ring patterns, or spotty rings, are visible in the SAED photos of the ABW-10 samples. The values in the standard data (JCPDS card no. 01-075-2187) and (JCPDS card no. 06-0505) are in good agreement with the measured inter-planar spacing (d_{hkl}) from SAED patterns (Fig. 4c). The (310), (211), (200), (320), (220), and (210) planes are recognized as the diffraction rings, arranged from inner to outer, and they clearly show the presence of both semiconductor crystals. Once more, we examined the spacings between neighbouring lattice fringes and found that they were 0.28 nm and 0.27 nm, respectively. These values matched the d-spacings of the (220) WO$_3$ and (210) Ag$_3$PO$_4$ nanoparticle planes, indicating a high degree of particle connectivity on the polymer surface.[26] We can identify the heterostructure nanocomposite's polycrystallinity (Fig. 4d) using the ABW-10 composite's SAED array. The concentric ring pattern of the ABW-10 composite is attributed to the planes of the two semiconductors on the biochar layer surface.[25,26]

3.3. Optical analysis and band gap determination

The optical absorption characteristics of WO$_3$, Ag$_3$PO$_4$, and the ternary composite ABW-10 were systematically examined using UV–vis diffuse reflectance spectroscopy (DRS), as illustrated in Fig. 5a–c. The results indicate that WO$_3$ and Ag$_3$PO$_4$ exhibit significant absorption within the visible light spectrum, which

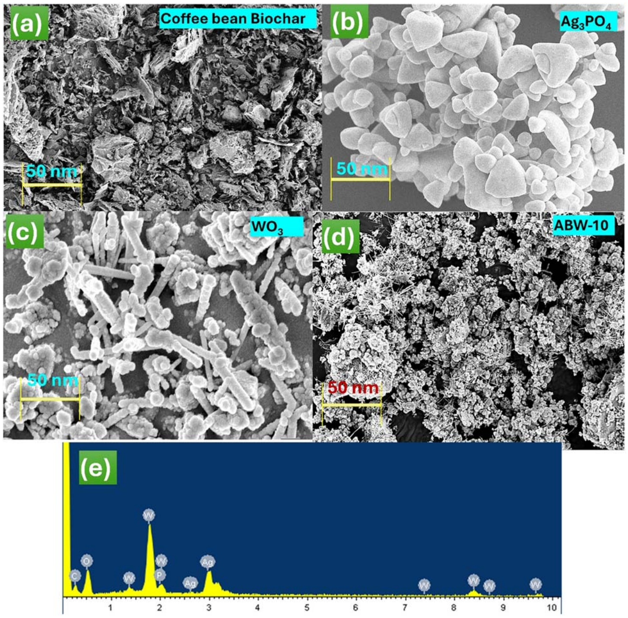

Fig. 2 SEM image of the (a) biochar, (b) Ag_3PO_4, (c) WO_3, (d) ABW-10, and (e) EDS of ABW-10.

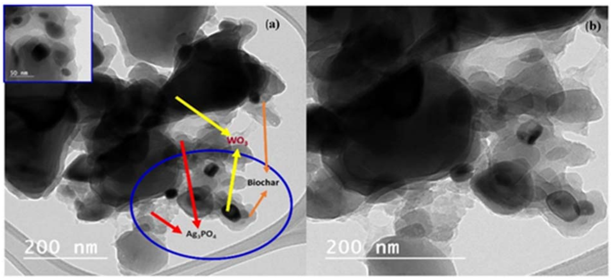

Fig. 3 TEM analysis of (a) close integration of WO_3, Ag_3PO_4, and biochar in ABW-10, (b) uniform distribution of particles in ABW-10 composite.

is further enhanced upon the incorporation of biochar and Ag_3PO_4 onto the WO_3 surface. The resulting ABW-10 heterostructure photocatalyst demonstrated a broader absorption range spanning the entire solar spectrum (200–800 nm), surpassing the individual components. This enhancement in optical absorption, particularly in the visible region, suggests improved light-harvesting efficiency, which is critical for photocatalytic applications. Furthermore, photoluminescence (PL) spectroscopy (Fig. 4h) was employed to evaluate charge carrier behavior under photon excitation at $\lambda_{ex} = 420$ nm. The observed reduction in PL intensity upon the incorporation of biochar and Ag_3PO_4 indicates suppressed radiative recombination of photogenerated electron–hole pairs. The lowest PL intensity recorded for ABW-10 indicates enhanced charge separation and suppressed electron–hole recombination, which contributes to its improved photocatalytic performance.

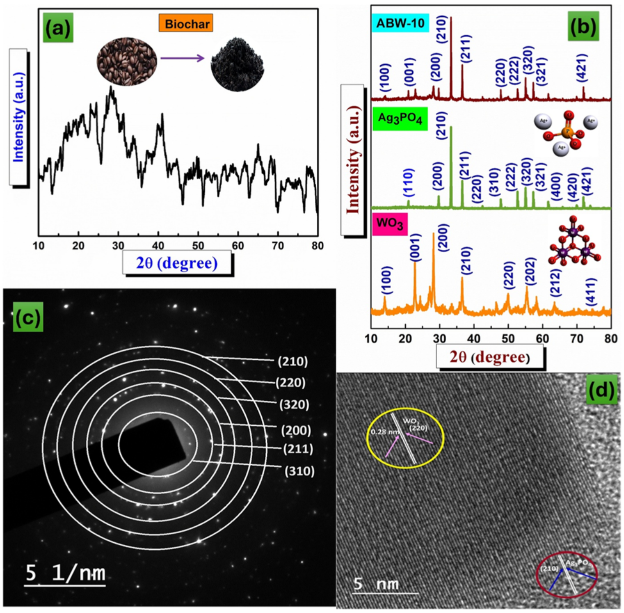

Fig. 4 XRD of (a) biochar, and (b) WO_3, Ag_3PO_4, and ABW-10 catalyst, (c) corresponding HRTEM analysis and SAED pattern of ABW-10, and (d) polycrystallinity nature of ABW-10 composite.

The structural and functional group analysis of the synthesized catalysts was further investigated using Fourier transform infrared (FTIR) spectroscopy, as presented in Fig. 5d–g. The FTIR spectrum of ABW-10 exhibits distinct absorption bands at approximately 3444 cm^{-1}, 2361 cm^{-1}, 1656 cm^{-1}, and 866 cm^{-1}, corresponding to O–H stretching, C≡C stretching, PO_4^{3-} stretching, and P–O–P stretching vibrations, respectively, confirming the presence of characteristic functional groups within the composite. Additionally, a broad peak at 817 cm^{-1} was attributed to W–O–W stretching vibrations, further validating the incorporation of WO_3. In the 900–1100 cm^{-1} region, a narrow broad band was identified, consistent with the vibrational features of WO_3.[18] The FTIR spectrum of pristine Ag_3PO_4 displayed characteristic peaks at 3353 cm^{-1} and 866 cm^{-1}, corresponding to asymmetric O–H stretching and O═P–O bending vibrations, respectively. For the coffee bean biochar, characteristic absorption peaks at 784 cm^{-1}, 1670 cm^{-1}, 2361 cm^{-1}, and 3430 cm^{-1} were assigned to C–H stretching, C═O stretching, C≡C stretching, and O–H stretching vibrations.[17] The presence of these functional groups and bonding interactions in the ABW-10 composite confirms the successful formation of the heterostructure catalyst, demonstrating its structural integrity and suitability for enhanced photocatalytic applications.

The band gap energy (E_g) of a semiconductor can be determined by extrapolating the linear portion of the $(\alpha h\nu)^n$ *versus* $h\nu$, as depicted in Fig. 5a–c. The calculated band gap values for Ag_3PO_4, WO_3, and the ABW-10 composite were found to be 2.4 eV, 2.85 eV, and 2.1 eV, respectively. The band gap values of WO_3 and Ag_3PO_4 align well with previously reported data, affirming the reliability of the measurements. Notably, the incorporation of biochar in ABW-10 resulted in a significant reduction in the band gap energy, with a decrease of 0.3 eV compared to Ag_3PO_4 and 0.75 eV compared to WO_3. This band

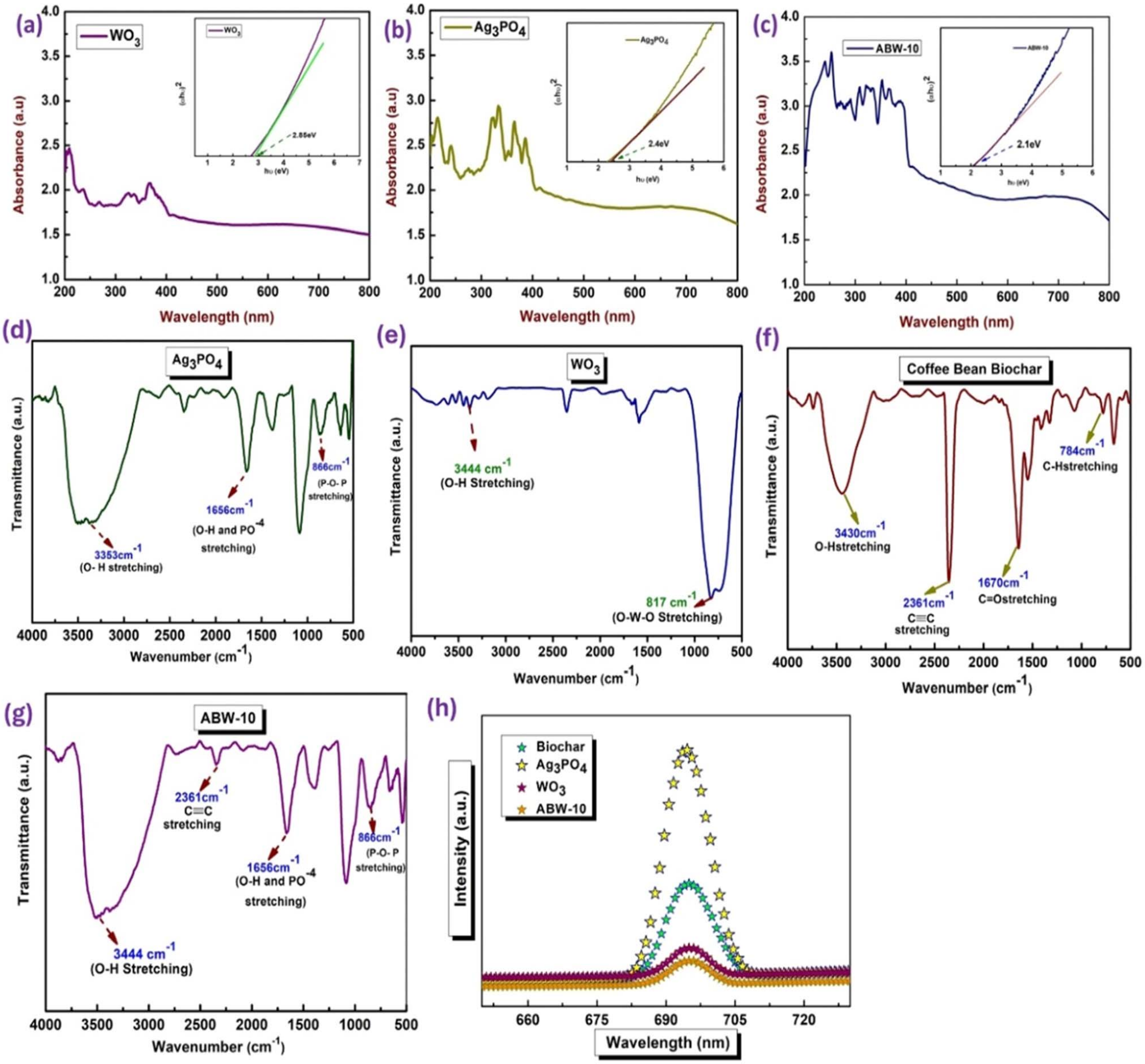

Fig. 5 UV-vis DRS spectra and inset Tauc plots of (a) WO_3, (b) Ag_3PO_4 and (c) ABW-10, FTIR spectra of (d) Ag_3PO_4, (e) WO_3, (f) coffee bean biochar and (g) ABW-10 nanocomposite and (h) PL spectra of biochar, Ag_3PO_4, WO_3 and ABW-10.

gap narrowing suggests enhanced electronic interactions within the heterostructure, primarily due to biochar's role as an electron shuttle, facilitating charge carrier mobility. The morphological analysis further reveals that the uniform dispersion of Ag_3PO_4 and WO_3 nanoparticles on biochar sheets forms conductive pathways throughout the composite matrix, thereby improving charge separation and transport. Furthermore, the unique surface properties of biochar contribute to the reduction in band gap energy by promoting an efficient electrical connection between WO_3 and Ag_3PO_4 within the Z-Scheme system.

The surface chemical states of the ABW-10 composite were further analysed using X-ray photoelectron spectroscopy (XPS), with all binding energies calibrated to the C 1s peak at 285 eV. The XPS spectrum of WO_3 nanorods, as shown in Fig. 6c, exhibits characteristic peaks at 35.0 eV and 36.7 eV, which correspond to the W $4f_{7/2}$ and W $4f_{5/2}$ orbitals of W^{6+}, respectively. Additionally, a peak at 530.5 eV is attributed to the lattice oxygen in the WO_3 nanorods, Fig. 6d, further confirming the oxidation state of tungsten.[27] The XPS spectrum of silver (Fig. 6a) displays distinct peaks at 369 eV and 375 eV, corresponding to the Ag $3d_{5/2}$ and Ag $3d_{3/2}$ binding energies, respectively, confirming the presence of Ag^+ ions in the composite. The absence of any detectable peaks related to metallic Ag^0 indicates that no reduction to elemental silver occurred during the synthesis, which aligns well with X-ray diffraction (XRD) results. Furthermore, the P 2p scan (Fig. 6b) shows a binding energy peak at 133.5 eV, corresponding to the

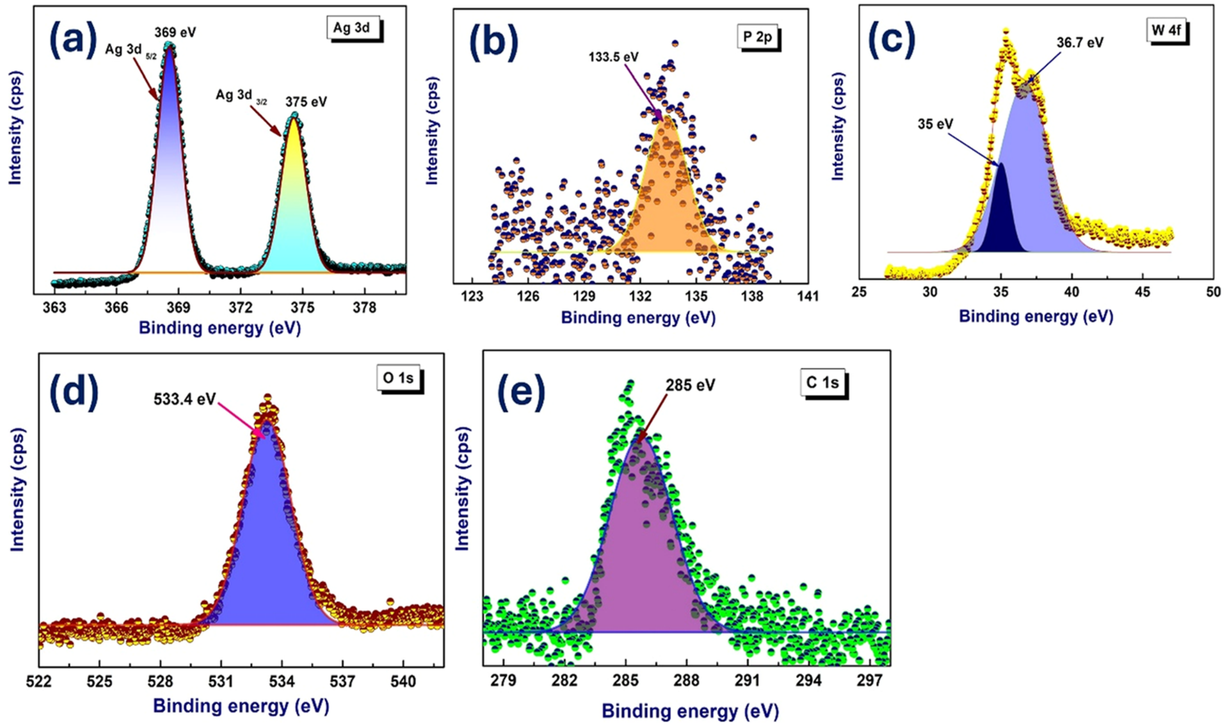

Fig. 6 XPS spectra of ABW-10 composite having (a) Ag 3d, (b) P 2p, (c) W 4f, and (d) O 1s, and (e) C 1s.

PO_4^{3-} species, verifying the incorporation of phosphate groups within the composite structure.[28] These results confirm the successful formation of the ABW-10 hybrid composite, demonstrating the effective integration of WO_3, Ag_3PO_4, and biochar in the synthesized material.

3.4. Contaminant removal analysis

The photocatalytic activity of various catalysts, including Ag_3PO_4, WO_3, biochar, and the synthesized ABW-10 composite, was systematically investigated for the degradation of the pesticide chlorpyrifos (CPF) and the antibiotic ciprofloxacin (CPX) under visible-light irradiation. Prior to light exposure, all samples were allowed to reach adsorption–desorption equilibrium in dark conditions. The photocatalytic efficiency of both individual catalysts and the ABW-10 composite was evaluated, as depicted in Fig. 7a and b. Comparative analysis revealed that ABW-10 exhibited superior photo-mineralization efficacy compared to its neat counterparts, highlighting its enhanced catalytic properties. It was found from the experimental analysis that the photodegradation of CPF without using photocatalyst ABW-10 is negligible less than 10% as shown in Fig. 7c.

Further investigations into the degradation efficiency were conducted using varying concentrations of CPF and CPX (10–100 ppm) over different time intervals (Fig. 8c and d). These experiments demonstrated that complete photodegradation of a 50 mg L^{-1} CPF and CPX solution was achieved within 60 minutes using an ABW-10 catalyst dose of 100 mg. However, an increase in CPF and CPX concentration led to a reduction in degradation efficiency, likely due to molecular aggregation at the active catalytic sites. This aggregation may hinder light penetration and interfere with the separation of photogenerated electron–hole (e^-/h^+) pairs, thereby reducing the overall photocatalytic degradation rate.

The UV-visible spectral scans (Fig. 8a and b) illustrate the temporal evolution of CPX and CPF concentrations during the degradation process. Notably, rapid degradation kinetics were observed (Fig. 8e and f), with CPX achieving nearly complete degradation within 60 minutes of irradiation, and CPF following a similar trend. The absence of any noticeable shift in the absorbance band throughout the degradation process indicates that CPF and CPX were mineralized into smaller, environmentally benign products such as CO_2 and ethene rather than merely breaking down into smaller organic fragments. Moreover, a recyclability test conducted over five successive cycles using a 50 mg L^{-1} CPX solution demonstrated only a marginal decrease in photocatalytic activity, underscoring the stability and reusability of ABW-10.

The degradation kinetics followed a first-order reaction model, as confirmed by high correlation coefficient (R^2) values. The degradation kinetics were plotted as $\ln(C_0/C_t)$ *versus* time (t) based on eqn (1),

$$\ln C_0/C_t = kt \tag{1}$$

where 'k' represents the rate constant, and 'C_0' and 'C_t' denote the initial and final concentrations of CPF or CPX at time t, respectively. This strong adherence to the first-order kinetic model further validates the efficiency of ABW-10 in the photocatalytic mineralization of CPX and CPF. In contrast to individual catalysts, the ABW-10 composite exhibited markedly

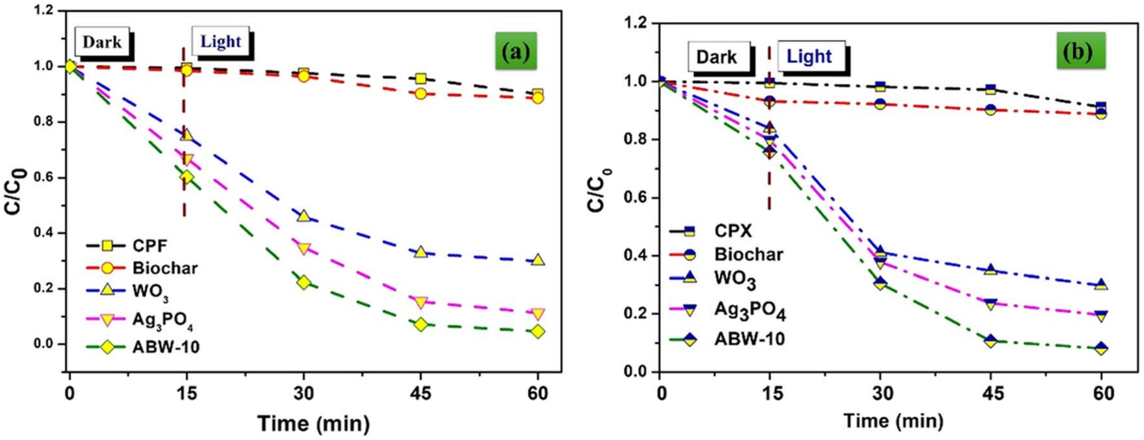

Fig. 7 Comparative photodegradation analysis of (a) ciprofloxacin, and (b) chlorpyrifos using biochar, WO_3, Ag_3PO_4, and ABW-10 composite.

enhanced reusability characteristics. The inherent susceptibility of pure Ag_3PO_4 to surface corrosion, resulting in degradation rates of 60–80% for CPX (at 50 ppm) and limited recycling potential, posed a significant challenge. Consequently, numerous investigations were undertaken to mitigate this self-corrosion propensity through surface modifications and doping strategies, including cobalt ferrite, PmAP doping, and facet engineering of Ag_3PO_4.[26] This study effectively addressed the corrosion inhibition of the Ag_3PO_4 structure within the ABW-10, consequently augmenting the recycling capability of the catalyst. In order to evaluate the adsorption efficiency of the individual components and the ABW-10 composite, batch adsorption experiments were conducted using CPF and CPX as target pollutants. Each adsorbent (biochar, WO_3, Ag_3PO_4, and ABW-10) was tested at a dosage of 0.1 g in a 100 mL solution containing 20 mg L^{-1} of CPF or CPX under dark conditions for 60 minutes to ensure adsorption–desorption equilibrium. As illustrated in Fig. 8g, the adsorption capacities of the materials varied significantly. Biochar exhibited moderate adsorption with 15.8 mg g^{-1} for CPF and 13.4 mg g^{-1} for CPX, attributed to its porous structure and abundant surface functional groups. WO_3 and Ag_3PO_4 demonstrated comparatively lower adsorption capacities, indicating limited surface interactions with the pollutants. Notably, the ABW-10 composite showed the highest adsorption efficiency, with 19.3 mg g^{-1} for CPF and 16.7 mg g^{-1} for CPX.[28]

3.5. LC-MS analysis

This study comprehensively investigated the photocatalytic degradation pathways of chlorpyrifos (CPF) and ciprofloxacin (CPX) using LC-MS analysis, which enabled the identification of intermediate and final degradation products. The LC-MS spectra revealed distinct mass signals for CPF (*m*/*z* 351, 170, 197, 239, 177, 114, 97, and 28) and CPX (*m*/*z* 331, 259, 229, 265, 212, 58, and 44), indicating the presence of both parent compounds and their degradation intermediates as shown in Fig. 1S and 2S (ESI†) respectively. Scavenging studies confirmed that hydroxyl radicals ($^{\bullet}OH$) and photogenerated holes (h^+) were the primary active species responsible for breaking down CPF and CPX into smaller by-products. The photocatalytic mechanism involved the excitation of CPF and CPX molecules, leading to electron transfer into the conduction band of ABW-10 and the subsequent formation of cationic radicals. These radicals interacted with oxygen species, producing oxidized intermediates that further degraded into aldehydes and carboxylic acids before complete mineralization into CO_2. The LC-MS spectra at the end of the reaction displayed molecular ion signals at lower *m*/*z* values, corresponding to CO_2, ethanol, ethene, and other minor organic species, confirming the effective degradation and mineralization process.

3.6. Photocatalytic mechanism

The Z-scheme photocatalytic mechanism of ABW-10 involving WO_3, Ag_3PO_4, and biochar under visible light irradiation presents an efficient pathway for enhanced degradation of pollutants such as chlorpyrifos (CPF) and ciprofloxacin (CPX). Mott–Schottky analysis, carried out using Staircase Potential Electrochemical Impedance Spectroscopy (SPEIS) in a 1 M Na_2SO_4 electrolyte, revealed that WO_3 is an n-type semiconductor with a conduction band (CB) at −0.17 eV and a band gap of 2.85 eV, placing its valence band (VB) at +2.68 eV. Conversely, Ag_3PO_4, a p-type semiconductor, shows a CB at −1.65 eV with a band gap of 2.4 eV, yielding a VB at +0.75 as shown in Fig. 9a and b respectively.

Eqn (2) was utilized to determine the conversion between Ag/AgCl and RHE, with all potentials being referenced against the reversible hydrogen electrode (RHE).

$$E_{\mathrm{RHE}} = E_{\mathrm{Ag/AgCl}} + 0.059\mathrm{pH} + 0.197\ \mathrm{V} \tag{2}$$

Upon visible light illumination, both WO_3 and Ag_3PO_4 generate photoinduced electron–hole pairs. In the proposed direct Z-scheme system, electrons in the CB of WO_3 recombine with holes in the VB of Ag_3PO_4 through biochar, which acts as a solid-state electron mediator. This preserves the strong redox potentials of the remaining charge carrier electrons in the CB of Ag_3PO_4 (−1.65 eV) and holes in the VB of WO_3 (+2.68 eV) as

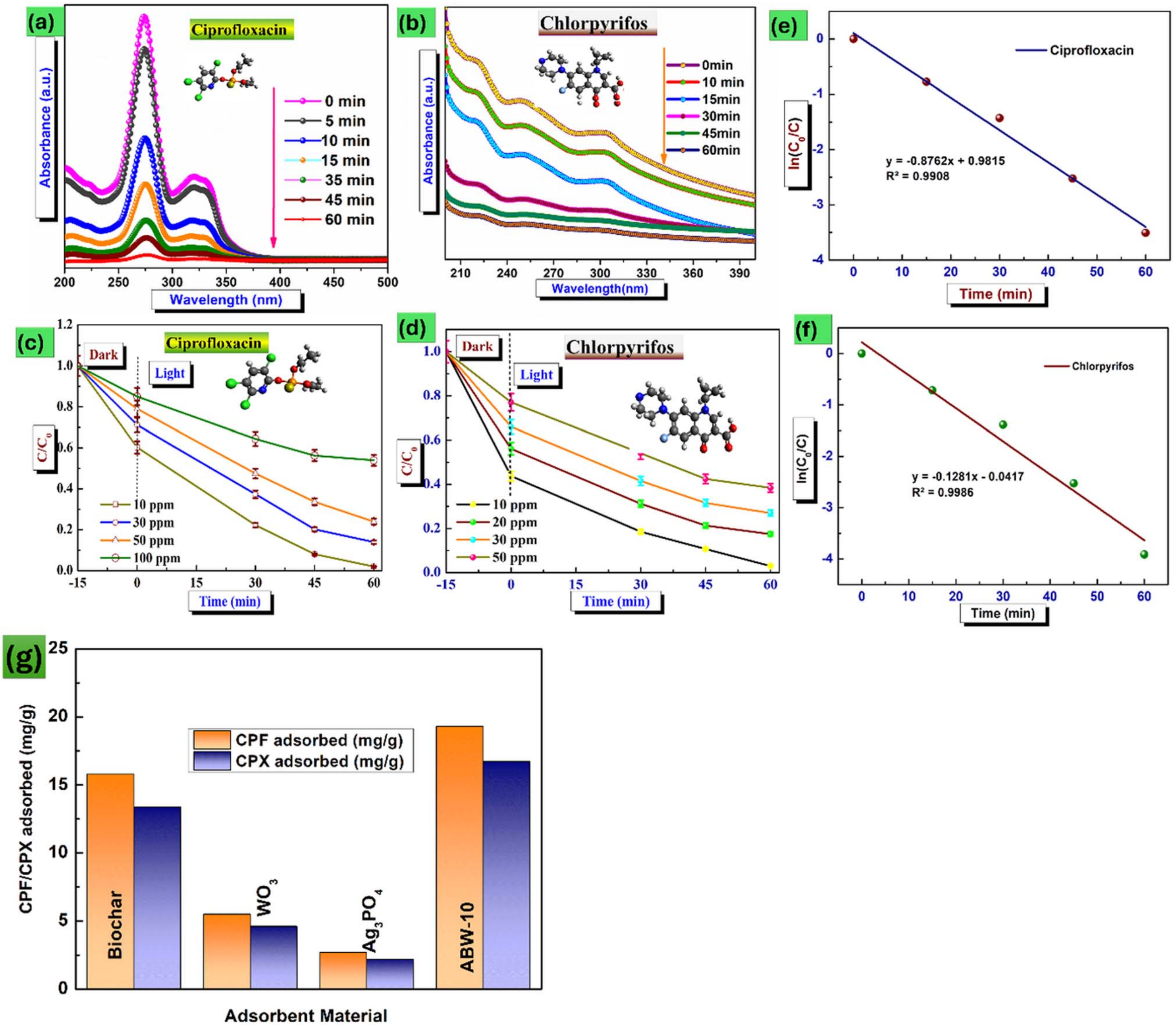

Fig. 8 (a and b) Photocatalytic activity of ABW-10 composites (catalyst dosage: 0.1 g) for (a) ciprofloxacin (50 mg L^{-1}), (b) chlorpyrifos (50 mg L^{-1}) pollutants degradation under visible light irradiation. (c and d) Photocatalytic activity of the ABW-10 composite with different concentrations of CPF and CPX, (e and f) Linear fitting of the visible light degradation profiles to the first-order kinetic model of CPF (30 mg L^{-1}) and CPX (20 mg L^{-1}) in the presence of the ABW-10 catalyst, (g) adsorption of CPF (20 mg L^{-1}) and CPX (20 mg L^{-1}) using biochar, WO_3, Ag_3PO_4, and ABW-10.

shown in Fig. 9. The valence band potential and the conduction band were computed using eqn (3).

$$E_{VB} = E_g + E_{CB} \tag{3}$$

Biochar's pivotal role stems from its partially graphitized structure, which enables high electrical conductivity and π-conjugation for rapid electron transfer. Its surface functional groups (*e.g.*, –OH, –COOH) aid in temporary electron capture and shuttling, reducing recombination. Furthermore, biochar's porous architecture and large surface area enhance contact between WO_3 and Ag_3PO_4, facilitating charge transfer across the interface. Its inherent redox-capacitive behaviour allows it to store and release electrons effectively, supporting stable charge carrier dynamics even under fluctuating light conditions.

The active species trapping experiments further validate the mechanism. When 1 mmol L^{-1} of scavengers were added benzoquinone (BQ) for $^{\bullet}O_2^-$, isopropanol (IPA) for $^{\bullet}OH$, and EDTA–Na_2 for h^+, the results showed a significant suppression in degradation efficiency upon BQ addition, confirming the major role of superoxide radicals ($^{\bullet}O_2^-$). IPA addition resulted in a ~35% reduction in CPX degradation, implicating $^{\bullet}OH$ radicals in the degradation process, while EDTA–Na_2 had minimal effect, indicating a lesser contribution from holes, as shown in Fig. 9d. In this Z-scheme configuration, the retained electrons in the CB of Ag_3PO_4 reduce adsorbed O_2 to generate $^{\bullet}O_2^-$ radicals, while the holes in the VB of WO_3 directly oxidize pollutants such as CPF and CPX through the hydroxyl radical ($^{\bullet}OH$). This synergistic charge separation, facilitated by biochar, enables efficient utilization of reactive oxygen species and strong

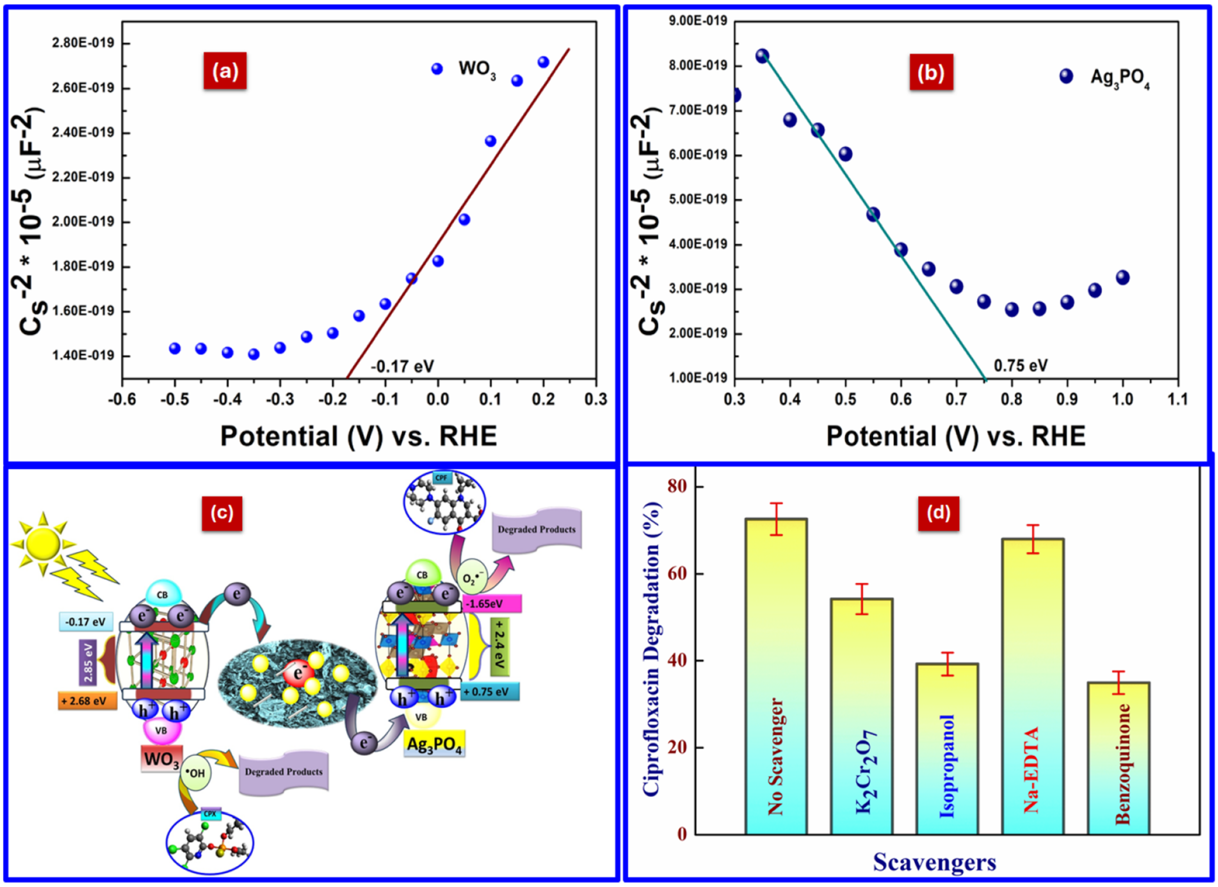

Fig. 9 (a) Mott–Schottky of WO_3 and (b) Ag_3PO_4, (c) A plausible mechanism of Z-scheme system e^-/h^+ pair transfer in ABW-10 under UV-Vis illumination of light, and (d) scavengers trapping experiments for photodegradation of ciprofloxacin by ABW-10.

oxidative holes, thereby enhancing the photocatalytic degradation of environmental contaminants.

3.7. Antimicrobial study

The antibacterial activity of ABW-10, WO_3, Ag_3PO_4, and biochar was systematically evaluated against *E. coli* and *S. aureus* using the agar well diffusion assay, revealing a concentration-dependent inhibitory effect. Among the tested materials, ABW-10 nanoparticles exhibited the highest antibacterial efficacy, with a zone of inhibition (ZOI) of 22 mm against *E. coli* and 19 mm against *S. aureus* at the maximum concentration of 1000 mg mL^{-1}. As illustrated in Fig. 10a–d, from Fig. 10e, the ZOI for individual components against *E. coli* was recorded as 3 mm for biochar, 11 mm for Ag_3PO_4, and 10 mm for WO_3, while for *S. aureus*, the ZOI values were 2 mm, 9 mm, and 8 mm, respectively. These results underscore the superior antibacterial performance of ABW-10, likely due to the synergistic effect of its

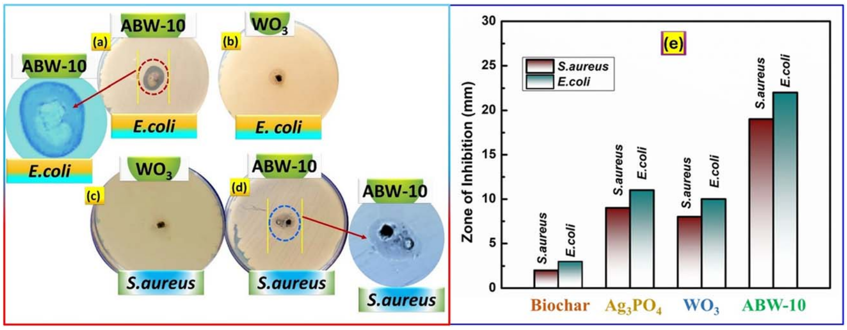

Fig. 10 Zone of inhibition at concentration of 1000 μg mL^{-1} in *Escherichia coli* (*E. coli*) with ABW-10 (a), WO_3 (b) and in *S. aureus* (*S. aureus*) WO_3 (c) and ABW-10 (d) and comparative study of individual catalyst ZOI at concentration of 1000 μg mL^{-1} using Gram negative (*E. coli*) and Gram positive (*S. aureus*).

Table 1 Comparative study of zone of inhibition (ZOI) for different semiconductors

	ZOI		
Hybrid material	*S. aureus*	*E. coli*	References
Copper oxide nanoparticles	14.5	9.33	29
Chitosan–silver nanoparticles (CS–AgNPs)	—	10	30
Methanol silver nanoparticles (SNPs)	14.33	10.33	31
AgNP-embedded guar gum/gelatin nanocomposite	13	12.5	32
Copper–silver–titanium oxide nanocomposite (Cu–Ag–TiO_2)	15	19	33
Magnesium/zinc oxide	19	15	34
ABW-10	19	22	This work

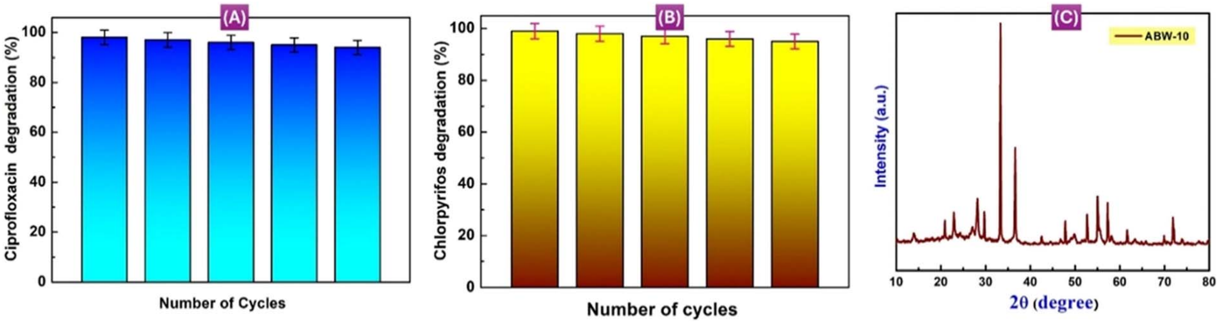

Fig. 11 Recyclability of photodegradation of (a) ciprofloxacin, and (b) chlorpyrifos of ABW-10 composite after the 5th cycle.

composite constituents. A comparative ZOI against Gram-positive and Gram-negative bacteria has been shown in Table 1. Furthermore, the comparative analysis presented in Table 1 highlights the relative antibacterial effectiveness of these photocatalysts, reinforcing the potential of ABW-10 as a promising antimicrobial agent.

3.8. Reusability analysis

The stability and recyclability of the catalyst used in photocatalytic processes are critical factors that determine their economic viability. In this case, five consecutive cycles of the same experimental setup were used to thoroughly assess the stability and recyclability of the ABW-10 composite. The results, as shown in Fig. 11a and b, indicate that the composite's degradation percentage remained relatively constant even after five cycles, indicating its strong durability during the CPX and CPF degradation process. Moreover, an investigation using powder X-ray diffraction (PXRD) after the fifth cycle, as shown in Fig. 11c, which confirms the ABW-10 catalyst's continued stability.

4. Conclusion

This study demonstrates the promising potential of utilizing biochar as an electron mediator in a Z-scheme system photocatalytic system, particularly in conjunction with WO_3 and Ag_3PO_4. The synthesized WO_3/Ag_3PO_4/biochar heterostructure, notably the ABW-10 catalyst, exhibited exceptional performance in the mineralization of organic contaminants under visible light irradiation. Through comprehensive characterization techniques, including PL spectroscopy, XRD, FTIR, and SEM/TEM morphological analysis, it was confirmed that the ABW-10 heterostructure possessed favourable properties such as reduced charge carrier recombination, abundant active sites, and intimate interfaces between components, facilitating rapid electron–hole pair transmission and extended charge carrier lifetime. The enhanced photocatalytic activity of the ABW-10 heterostructure, leading to complete degradation of the antioxidant ciprofloxacin pollutant and noxious chlorpyrifos in 60 minutes, surpasses that of individual WO_3 and Ag_3PO_4 catalysts. This enhanced performance can be attributed to the synergistic effects and strong interaction among the components within the composite heterostructure. Moreover, the stability of the heterostructure Z-scheme system photocatalysts under visible light irradiation further underscores their potential for practical applications in the treatment of antibiotic and pesticide containing wastewater and other environmental pollutant cleanup processes. In summary, the ABW-10 catalyst exhibits favourable characteristics such as proper Z-scheme system band alignment, efficient electron–hole migration, and high light absorption capacity, making it a promising candidate for advancing photocatalysis-based solutions for energy and environmental waste remediation. Continued research in this area holds great promise for addressing pressing environmental challenges and advancing sustainable technology solutions.

Consent to participate and publish

All the authors consented to participate in drafting and publishing this manuscript.

Data availability

The data that support the findings of this study are available from the corresponding author [Behera, A. K.] upon reasonable request.

Author contributions

Debasis Nanda: Writing – original draft, data curation, and visualization; Chirasmayee Mohanty: writing and editing the original draft, visualization, conceptualization; Amrita Priyadarsini: software, formal analysis, data curation, methodology; Nigamananda Das: software, formal analysis, data curation; Manjusri Misra: Software, formal analysis, data curation, methodology; Amar K. Mohanty: data curation and formal analysis; Ajaya K. Behera: methodology, supervision.

Conflicts of interest

There are no conflicts to declare.

Acknowledgements

Debasis Nanda and Chirasmayee Mohanty have contributed equally. We are grateful to the Department of Chemistry, Utkal University, Bhubaneswar for allowing the smooth conduct of experiments. We are also grateful to Central Instrumentation Facility, Odisha University of Technological Research, Bhubaneswar for conducting scanning electron microscopy for the samples.

References

1 A. Anjitha, A. Shijina, K. V. Ajayan, S. Swaminathan, I. M. C. Lo and K. Sridharan, Combating eukaryotic and prokaryotic harmful algal blooms with visible-light driven BiOBr$_x$I$_{1-x}$/MFe$_2$O$_4$/g-C$_3$N$_4$ (M = Co & Ni) recyclable photocatalysts, *Environ. Sci.: Nano*, 2025, **12**, 262–275.

2 Y. Li and J. Wang, 2D/2D *Z* -scheme WO$_3$/g-C$_3$ N$_4$ heterojunctions for photocatalytic organic pollutant degradation and nitrogen fixation, *Mater. Adv.*, 2024, **5**, 749–761.

3 C. Shen, Z. Song, Z. Qiu and R. Gao, Effects of pyrolysis temperature on drinking water treatment residual biochar properties and organophosphorus pesticides adsorption, *Chem. Pap.*, 2024, **78**, 5289–5299.

4 X. Liu, J. Zhou, G. Wang, D. Liu and S. Liu, Construction of Cu-Fe bimetallic oxide/biochar/Ag3PO4 heterojunction for improving photocorrosion resistance and photocatalytic performance achieves efficient removal of phenol, *Appl. Surf. Sci.*, 2022, **592**, 153307.

5 S. Dong, J. Dai, Y. Yang, A. Zada and K. Qi, Extended Interfacial Charge Transference in CoFe2O4/WO3 Nanocomposites for the Photocatalytic Degradation of Tetracycline Antibiotics, *Molecules*, 2024, **29**, 4561.

6 Z. Dou, C. Li, X. Ji, J. Lai, Q. Fu, H. Liu, S. Gong and J. Wu, Efficient degradation of tetracycline in wastewater by novel biochar-based photocatalytic materials: performance, photocatalytic mechanism and degradation pathways, *Res. Chem. Intermed.*, 2025, **51**, 111–134.

7 E. Weidner, E. Karbassiyazdi, A. Altaee, T. Jesionowski and F. Ciesielczyk, Hybrid Metal Oxide/Biochar Materials for Wastewater Treatment Technology: A Review, *ACS Omega*, 2022, **7**, 27062–27078.

8 H. Dhila, A. Bhapkar and S. Bhame, Metal oxide/biochar hybrid nanocomposites for adsorption and photocatalytic degradation of textile dye effluents: A review, *Desalin. Water Treat.*, 2025, **321**, 101004.

9 V. Son Tran, H. Hao Ngo, W. Guo, T. Ha Nguyen, T. Mai Ly Luong, X. Huan Nguyen, T. Lan Anh Phan, V. Trong Le, M. Phuong Nguyen and M. Khai Nguyen, New chitosan-biochar composite derived from agricultural waste for removing sulfamethoxazole antibiotics in water, *Bioresour. Technol.*, 2023, **385**, 129384.

10 C. Mohanty, A. Samal, A. K. Behera and N. Das, Poly-m-aminophenol/CoFe2O4 (p–n) heterojunction: Sustainable decontamination of BPA, ciprofloxacin pollutants from water and its study of antimicrobial performance, *J. Water Process Eng.*, 2024, **65**, 105821.

11 Z.-W. Ma, H.-Q. Liu and Q.-F. Lü, Porous biochar derived from tea saponin for supercapacitor electrode: Effect of preparation technique, *J. Energy Storage*, 2021, **40**, 102773.

12 H. S. Shahraki, R. Bushra, N. Shakeel, A. Ahmad, Quratulen, M. Ahmad and C. Ritzoulis, Papaya peel waste carbon dots/reduced graphene oxide nanocomposite: From photocatalytic decomposition of methylene blue to antimicrobial activity, *J. Bioresour. Bioprod.*, 2023, **8**, 162–175.

13 Y. Liu, X. Dai, J. Li, S. Cheng, J. Zhang and Y. Ma, Recent progress in TiO$_2$ –biochar-based photocatalysts for water contaminants treatment: strategies to improve photocatalytic performance, *RSC Adv.*, 2024, **14**, 478–491.

14 A. P. Khedulkar, V. D. Dang, A. Thamilselvan, R. Doong and B. Pandit, Sustainable high-energy supercapacitors: Metal oxide-agricultural waste biochar composites paving the way for a greener future, *J. Energy Storage*, 2024, **77**, 109723.

15 K. Kadiya, S. B. Vuggili, U. K. Gaur and M. Sharma, Comparative photocatalytic dye and drug degradation study using efficient visible light–induced silver phosphate nanoparticles, *Environ. Sci. Pollut. Res.*, 2021, **28**, 46390–46403.

16 X. Feng, X. Li, B. Su and J. Ma, Two-step construction of WO3@TiO2/CS-biochar S-scheme heterojunction and its synergic adsorption/photocatalytic removal performance for organic dye and antibiotic, *Diamond Relat. Mater.*, 2023, **131**, 109560.

17 B. Armynah, D. Tahir, M. Tandilayuk, Z. Djafar and W. H. Piarah, Potentials of Biochars Derived from Bamboo Leaf Biomass as Energy Sources: Effect of Temperature and Time of Heating, *Int. J. Biomater.*, 2019, **2019**, 1–9.

18 S. Erdönmez, Y. Karabul, M. Kılıç, Z. Güven Özdemir and K. Esmer, Structural characterization and dielectric parameters of polyindole/WO$_3$ nanocomposites, *Polym. Compos.*, 2021, **42**, 1347–1355.

19 Z. Yuan, H. Huang, N. Li, D. Chen, Q. Xu, H. Li, J. He and J. Lu, All-solid-state WO3/TQDs/In2S3 Z-scheme heterojunctions bridged by Ti3C2 quantum dots for efficient removal of hexavalent chromium and bisphenol A, *J. Hazard. Mater.*, 2021, **409**, 125027.

20 A. Amirulsyafiee, M. M. Khan and M. H. Harunsani, Ag3PO4 and Ag3PO4–based visible light active photocatalysts: Recent progress, synthesis, and photocatalytic applications, *Catal. Commun.*, 2022, **172**, 106556.

21 S. Shenoy and K. Sridharan, Bismuth oxybromide nanoplates embedded on activated charcoal as effective visible light driven photocatalyst, *Chem. Phys. Lett.*, 2020, **749**, 137435.

22 E. Johnson, N. Reji, A. A, S. K and K. Sridharan, Boosting photocatalytic efficiency and nonlinear optical response of graphitic carbon nitride by infusing carbon nanotubes, *J. Mol. Struct.*, 2025, **1321**, 140089.

23 L. Liu, L. Ding, Y. Liu, W. An, S. Lin, Y. Liang and W. Cui, A stable Ag3PO4@PANI core@shell hybrid: Enrichment photocatalytic degradation with π-π conjugation, *Appl. Catal., B*, 2017, **201**, 92–104.

24 K. B. Singh, D. D. Upadhyay, N. Gautam, Snigdha, A. Gautam and G. Pandey, Sonochemical reassembling of Acacia nilotica bark extract mediated Mg doped WO3@g-C3N4 ternary nanocomposite: A robust nanophotocatalyst, *J. Photochem. Photobiol., A*, 2023, **441**, 114739.

25 M. Sultana, S. R. Mohapatra and Md. Ahmaruzzaman, Band gap engineering of Ag/CeO2/Co3O4@biochar composite with superior light harvesting for photocatalytic removal of Diclofenac and Naphthalene from effluents, *Clean Technol. Environ. Policy*, 2024, DOI: **10.1007/s10098-024-03105-5**.

26 C. Mohanty, A. Samal, A. K. Behera and N. Das, Poly Meta-Aminophenol (PmAP) as a Solid-State Electron Mediator in the Z-Scheme, Ag$_3$ PO$_4$/CoFe$_2$ O$_4$ Heterojunction: Mineralization of Highly Concentrated Bisphenol-A and Reactive Dyes Water Pollutants, *ACS Omega*, 2024, **9**, 19968–19981.

27 Y. Yang, H. Fu, F. Song, S. Yu, Z. Tang, K. Zhang, Q. Li, C. Yang, L. Zhang, J. Wang, Y. Pang, C. Wang, B. Liu, J. Chen and Q. Jing, A high-performance H2 gas sensor based on PtO*x* and PdO*y* co-decorating WO3 film, *New J. Chem.*, 2025, **49**, 5266–5278.

28 E. Johnson, A. Raj, S. Kottarathil, A. Johansson and K. Sridharan, Bismuth-rich Bi4O5Br2 anchored on g-C3N4 nanosheets: Enhanced visible-light performance for simultaneous photocatalytic degradation of emerging pollutants and spectroscopic insights, *Sep. Purif. Technol.*, 2025, **364**, 132521.

29 S. Z. S. Alvarez, K. R Abraham, R. D. T. Azurin, I. G. O. B. Bacani, C. A. G. Banaag, A. M. G. Bato, K. A. L. Budomo and P. R. Bremner, Antibacterial Activity of Green Synthesized Copper Oxide Nanoparticles Using Muntingia calabura Leaf Extracts against Staphylococcus aureus and Escherichia coli, *Asian J. Biol. Life Sci.*, 2024, **13**, 330–337.

30 S. Tharani, D. Bharathi and R. Ranjithkumar, Extracellular green synthesis of chitosan-silver nanoparticles using Lactobacillus reuteri for antibacterial applications, *Biocatal. Agric. Biotechnol.*, 2020, **30**, 101838.

31 H. Yousaf, A. Mehmood, K. S. Ahmad and M. Raffi, Green synthesis of silver nanoparticles and their applications as an alternative antibacterial and antioxidant agents, *Mater. Sci. Eng., C*, 2020, **112**, 110901.

32 N. Khan, D. Kumar and P. Kumar, Silver nanoparticles embedded guar gum/gelatin nanocomposite: Green synthesis, characterization and antibacterial activity, *Colloid Interface Sci. Commun.*, 2020, **35**, 100242.

33 J. Emima Jeronsia, R. Ragu, R. Sowmya, A. J. Mary and S. Jerome Das, Comparative investigation on Camellia Sinensis mediated green synthesis of Ag and Ag/GO nanocomposites for its anticancer and antibacterial efficacy, *Surf. Interfaces*, 2020, **21**, 100787.

34 V. Rajendran and R. Mekala, Effect of pure and REM: (Nd, Ce)-doped Dy2O3 NPs via hydrothermal method and their magnetic, optical, electrochemical, antibacterial and photocatalytic activities, *J. Alloys Compd.*, 2018, **741**, 1055–1069.